analytical chemistry

ARTICLE

pubs.acs.org/ac

Microfluidic Electrochemical Sensor Array for Characterizing Protein Interactions with Various Functionalized Surfaces

Peter H. Dykstra,[*,†] Varnika Roy,[‡,⊥] Christopher Byrd,[‡,§] William E. Bentley,[‡] and Reza Ghodssi[*,†,‡]

[†]MEMS Sensors and Actuators Laboratory (MSAL), Department of Electrical and Computer Engineering, Institute for Systems Research, [‡]Fischell Department of Bioengineering, [⊥]Graduate Program in Molecular and Cell Biology, and [§]Army Research Laboratory, University of Maryland, College Park, Maryland, United States

ABSTRACT: We present a unique microfluidic platform to allow for quick and sensitive probing of protein adsorption to various functionalized surfaces. The ability to tailor a sensor surface for a specific analyte is crucial for the successful application of portable gas and fluid sensors and is of great interest to the drug screening community. However, choosing the correct surface chemistry to successfully passivate against nonspecific binding typically requires repeated trial and error experiments. The presented device incorporates an array of integrated electrochemical sensors for fast, sensitive, label-free detection of these binding interactions. The layout of the electrodes allows for loading various surface chemistries in one direction while sensing their interactions with particular compounds in another without any cross-contamination. Impedance data is collected for three commonly used passivation compounds (mercaptohexanol, polyethylene glycol, and bovine serum albumin) and demonstrates their interaction with three commonly studied proteins in genetic and cancer research (cAMP receptor protein, tumor necrosis factor α, and tumor necrosis factor β). The ability to quickly characterize various surface interactions provides knowledge for selecting optimal functionalization for any biosensor.

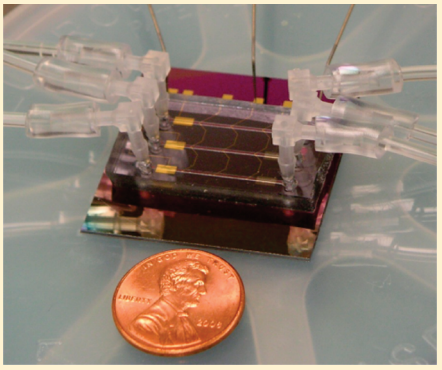

Clinical diagnostics is a quickly evolving field that can directly benefit from the next generation of biosensors. These sensors must provide fast; reliable; sensitive; and, most importantly, selective detection for a variety of biomolecular interactions. Most often, these interactions involve affinity-based binding of antibodies, DNA, and proteins.[1−5] Specifically, the detection of particular proteins is an important issue for both the drug screening community and for early diagnosis and has been a source of motivation for many recently reported biosensors.[6−10] The challenge with many of these biosensors is achieving an acceptable level of selectivity. The most common method for solving the selectivity issue is to use probe molecules with high affinity for a specific protein, such as DNA aptamers, antibodies, or double-stranded DNA, immobilized on the sensing surface;[7,11−13] however, the surface must be further protected against nonspecific binding through the use of passivation compounds. There has also been extensive research aimed at observing biomolecule adsorption to passivation compounds immobilized onto drug delivery systems and various other biomedical devices.[14−16] The adsorption kinetics of proteins to a vast array of surfaces and immobilized compounds has been debated and analyzed by many groups;[17−19] however, many research groups utilize methods that require the use of complicated measurement equipment, and in nearly all published examples of protein−surface characterizations, the tests can be performed only one at a time.

The most common technique for measuring protein adsorption to a surface with electrical measurements is to use a quartz crystal microbalance.[20−23] Adsorption of proteins to the functionalized surface of the resonator can be detected with very high precision from the change in resonance frequency. Although this technique is very sensitive, each resonator contains a single surface and can be tested only one at a time. This makes performing an array of tests a time-consuming task. Other electrical techniques commonly employed are cyclic voltammetry[24] and impedance-based methods;[25,26] however, these techniques also test a single sensor in an enclosed fixture during the experiment, which complicates high-throughput analysis.

Optical techniques such as surface plasmon resonance (SPR) have also been employed to detect protein adsorption.[14,25,27] With this technique, minor changes in surface dielectric properties on an electrode change the angle at which surface plasmon waves are generated from an incident beam of light. SPR has been used for many years for detecting binding and adsorption of various compounds; however, it requires expensive free-space optical equipment and difficult alignment of all the components. Other optical techniques, such as total internal reflection fluorescence, have been reported for protein adhesion characterization, but they requires labeling of the proteins with a fluorescent dye.[28] The labeling procedure can cause denaturation of some labile proteins.[29]

Received: April 1, 2011
Accepted: June 20, 2011
Published: June 20, 2011

To our knowledge, there has been little work done to characterize protein−surface interactions using a microfluidic device. Microfluidics provides the ability to pattern many sensors in a small footprint and drastically reduce the reagent costs. Here, we have utilized an array of electrochemical sensors integrated within microfluidic channels to allow for the probing of protein interactions with multiple functionalized surfaces. Although electrochemical measurements have been demonstrated previously in microfluidic channels,[30−32] to our knowledge, this is the first reported use of electrochemistry in a microfluidic device for the characterization of protein adhesion. Using microfluidic channels with integrated sensors allows for fast reaction times, low required sample volumes, and label-free detection of the interactions. Electrical-based detection has been implemented over optical or mechanical techniques due to its ease of fabrication and interfacing with multiple sensors in parallel.

The sensors are arranged to expose multiple functionalized sites without cross-contamination while allowing protein samples to interact with each surface. The device's various sensor surfaces are modified using three well-known passivation agents: mercaptohexanol (MCH), a thiolated polyethylene glycol (PEG), and bovine serum albumin (BSA). MCH is very commonly used to passivate sensing surfaces for both protein and DNA sensing, and PEG has been widely studied for its ability to resist protein adsorption.[33−36] BSA has been extensively used to passivate surfaces against nonspecific binding in a variety of biosensors.[37,38]

Three different proteins have been chosen to interact with the modified sensor surfaces: cAMP (cyclic adenosine monophosphate) receptor protein (CRP), tumor necrosis factor α (TNFα), and tumor necrosis factor β (TNFβ). CRP is a common gene regulator in bacteria and is the focus of many genetic and biochemical studies.[39,40] Both TNFα and TNFβ are used extensively in cancer related research as tumor markers.[41,42] The proteins are chosen to cover various biological applications to highlight the broader impact of this research. They are meant to provide a proof-of-concept operation of the device.

The microfabricated sensors are first characterized using cyclic voltammetry to ensure uniformity and cleanliness among the patterned electrodes. Each column of sensors is passivated with MCH, BSA, or PEG. Finally, each of the three proteins is flown over different sensor rows, which include each of the three passivation surfaces. Impedance spectroscopy data are collected for each sensor to characterize the interaction between each protein and each passivation surface. A Discussion section is included to further examine the complex interactions taking place at the electrode surface.

EXPERIMENTAL SECTION

A. Materials and Equipment. The cAMP receptor protein (CRP) was overexpressed in *Escherichia coli* BL21DE3 cells and purified via his-tag-based IMAC purification (immobilized metal affinity chromatography) and resulted in a final protein yield of 0.43 mg/mL in a 10 mM phosphate buffered saline (PBS) solution. The activity of the protein was verified through a gel shift assay that detects CRP's binding to the specific CRP oligonucleotide sequence. Tumor necrosis factor α, tumor necrosis factor β, 6-mercapto-1-hexanol, and bovine serum albumin were each purchased from Sigma-Aldrich (St. Louis, MO) and (1-mercapto-11-undecyl)tetra(ethylene glycol) was purchased from Asemblon Inc. (Redmond, WA). Both the MCH and PEG were diluted in 10 mM PBS. TNFα and TNFβ were each reconstituted in 10 mM PBS with added 0.1% BSA.

All electrochemical measurements were taken using a CHI660D potentiostat from CH Instruments (Austin, TX). The electrolyte used in all experiments was 10 mM PBS with 100 mM added NaCl and included 2.5 mM ferri-/ferrocyanide as a reversible redox couple.

B. Device Design. The platform is designed to include an array of addressable sensors. Each sensor consists of an electrode aligned within a microfluidic channel. Electrochemical measurements typically require a three-electrode setup: a working electrode, in which the relevant binding interactions occur; a reference electrode, acting as a stable potential reference; and a counter electrode, which collects the current between itself and the working electrode. To carry out the measurements, each channel must include a unique counter and reference electrode along with individually addressable working electrodes. It is also important that the area of the counter electrode exceed that of the working electrode. This works to maximize the changes in the current response of the system due to binding reactions at the working electrode. Gold is used for both the working and counter electrodes because of its high resistance to corrosion and high standard electrode potential of 1.52 V. Platinum is chosen for the reference electrode due to its relatively stable electrode potential and compatibility with microfabrication techniques. More complex aqueous electrodes, including Ag/AgCl and the saturated calomel electrode, yield better potential stability but are very difficult to integrate within a microfabricated device.

The device is designed with nine working electrodes patterned in a 3 × 3 grid. Each working electrode is a disk of 100 μm radius, and they are spaced 5 mm apart in the channel. The circular profile is used to reduce fringing effects at corners, which may result in an uneven concentration profile across the surface of the electrode. In addition, each column of working electrodes is electrically connected to reduce the number of outputs from nine down to three. This design choice becomes especially important for scaling the device up for future iterations to include a higher number of sensors.

Microfluidic channels are molded in polydimethysiloxane (PDMS, Slygard 184). The spacing of the sensors and the molded channels are designed so that the channels can be placed across the sensors, exposing each sensor column in its own unique channel. Each sensor column can be incubated with a different functionalization compound without any cross-contamination between the other channels. Afterward, the PDMS channels can be peeled off, rinsed, then rotated 90 degrees in-plane and placed back down over the patterned sensors. In this way, rows of sensors are exposed in each channel along with unique counter and reference electrodes. This process is demonstrated schematically in Figure 1.

C. Device Fabrication. The chips are patterned on a standard 4 in. silicon wafer with a 1 μm PECVD silicon dioxide top layer. The silicon dioxide provides insulation between electrodes and yields a stronger bond with the PDMS. Electrodes are patterned by first depositing 20 nm of chrome, followed by 200 nm of gold using DC sputtering across the wafer. The chrome acts as an adhesion layer for the gold onto the silicon dioxide surface. The working and counter electrodes are patterned using Shipley 1813 photoresist and gold and chrome etchant, respectively. The wafer is cleaned and an image-reversal photoresist AZ5214 is patterned to define the locations for the platinum reference electrodes. E-beam evaporation is used to deposit 40 nm of titanium

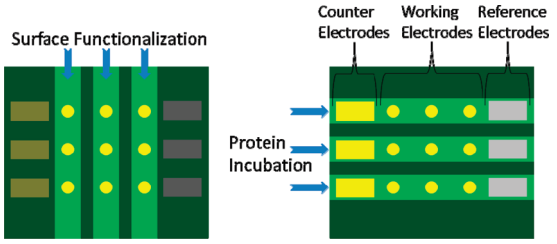

Figure 1. (a) The PDMS channels are aligned to expose columns of working electrodes to be functionalized by different compounds. (b) After functionalization, the PDMS channels are lifted, rotated, and placed back down to align counter and reference electrodes within separate rows of working electrodes.

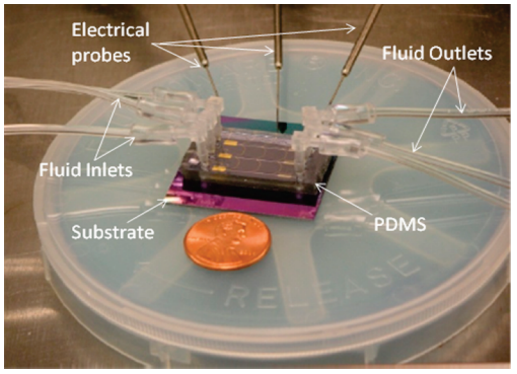

Figure 2. Photograph of the packaged device with fluidic I/O connections under test using micropositioning probes. The substrate is a silicon chip with a top layer of thermally grown silicon dioxide.

followed by 200 nm of platinum. The titanium acts as the adhesion layer for the platinum to the silicon dioxide. The metal is lifted off by placing the wafer in an ultrasonic acetone bath, leaving behind the patterned reference electrodes.

Afterward, the wafer is cleaned using a piranha solution of 4:1 sulfuric acid/hydrogen peroxide to remove any organic contaminants on the working electrodes. Care must be taken during this step, since the piranha will also slowly etch the titanium adhesion layer, so the wafer should not be exposed to the solution any longer than 10−15 s. Each chip measuring 3.5 cm ×3.5 cm is finally diced from the wafer.

A separate silicon wafer is used to pattern the mold for the PDMS channels. The mold is patterned using SU-8 50 from Microchem (Newton, MA, USA). The SU-8 is spun to a thickness of 100 um and patterned to form the parallel microfluidic channels. PDMS is mixed with a polymer/curing agent ratio of 10:1 and degassed in a vacuum bell jar. The polymer is poured over the SU-8 mold and cured in a furnace at 80 C for 20 min. Afterward, the PDMS channels are carefully peeled from the mold wafer, and holes with a radius of 1 mm are punched through the PDMS to create fluid inlet and outlet ports. The PDMS is then cut to dimensions slightly smaller than that of the patterned chip, and the electrodes are visually aligned to lie within all three of the channels. The PDMS creates a solid reversible bond with the silicon dioxide surface, which exhibits no leaking through testing. Plastic elbow connectors coupled with Tygon flexible tubing are placed in the PDMS inlets and outlets to complete the packaging. The packaged device under test is shown in Figure 2.

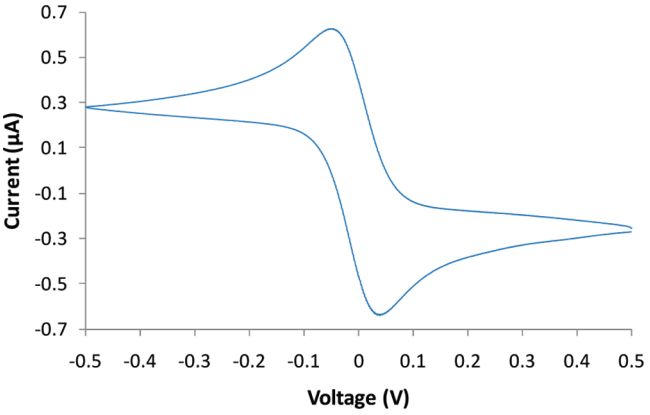

Figure 3. Typical cyclic voltammetry result for a clean surface on one of the nine sensors in the device. The scan was taken using 2.5 mM ferri-/ferrocyanide redox couple in 10 mM PBS + 100 mM NaCl.

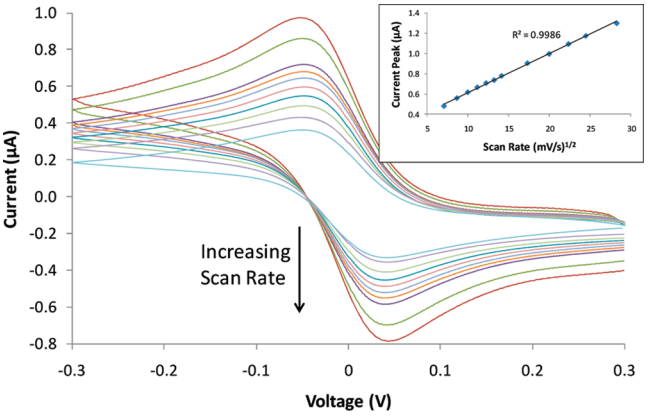

Figure 4. Cyclic voltamgrams with increasing scan rates from 25 to 400 mV/s. (inset) Linear relationship observed between the reduction current peak amplitude and the square root of the scan rate.

D. Sensor Characterization. After fabrication, the sensors were each tested to ensure uniformity and cleanliness. Each channel was filled with PBS electrolyte containing the ferri-/ferrocyanide redox couple. Cyclic voltammetry (CV) scans from 0.3 to −0.3 V were performed at each of the nine sensors. A representative plot for one is shown in Figure 3.

Each sensor exhibits very similar peak separation (0.087 ± 0.004 V) and peak amplitude for both the oxidation (−799 ± 9.8 nA) and reduction (746 ± 9.8 nA) peaks. The oxidation and reduction potentials of the ferri-/ferrocyanide couple are 0.037 ± 0.002 V and −0.05 ± 0.002 V, respectively, for each of the nine sensors, which demonstrates the relative potential stability of the platinum reference electrodes in each channel.

The cleanliness of the electrode surface can be observed electrochemically from how reversible the oxidation and reduction reactions of the ferri-/ferrocyanide couple are. The CV peak current for a reversible reaction can be calculated using the Randles−Sevcik equation, below,

$$i_p = (2.69 \times 10^5) n^{3/2} A D^{1/2} C v^{1/2} \quad (1)$$

where n is the number of electrons transferred per ion in solution, A is the area of the working electrode, D is the diffusion

Scheme 1. Randles Equivalent Circuit Model for Complex Impedance of the Electrode System[a]

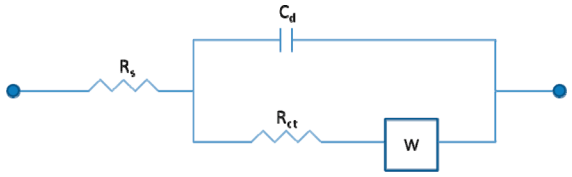

[a] The model contains the solution resistance (R_s); double layer capacitance in an ionic media (C_d); charge transfer resistance (R_{ct}); and the Warburg impedance (W), which is frequency-dependent and models the effects of diffusion.

coefficient for the redox compound, C is the concentration of the redox species, and v is the scan rate in V/s. From 1, for a reversible redox reaction, the peak current should be linearly proportional to the square root of the scan rate. Figure 4 displays the CV response for one of the sensors at scan rates varying from 25 to 400 mV/s. The inset graph displays the linear relationship between the peak current and the square root of the scan rate with an R^2 value very close to unity (refer to the figure). It is also important to observe from the cyclic voltagrams that the oxidation and reduction potentials at each scan rate are the same, which is indicative of a reversible reaction and a clean electrode surface.

E. Surface Preparation. Solutions of 1 mM MCH, 1% BSA, and 10 μM PEG are dissolved in PBS to be used for testing. The PDMS channels are placed on the chip so that the nine working electrodes are exposed within the three channels. Using separate 1 mL syringes, channel 1 is filled with the solution containing the MCH, channel 2 is filled with the solution containing BSA, and channel 3 is filled with the solution containing PEG. The solutions are incubated over the working electrodes for 1 h to allow for the compounds to either bind to the gold surface via their thiol group (in the case of MCH and PEG) or adsorb to the surface (in the case of the BSA). Previous empirical studies performed by our group were used to find that 1 h is a sufficient amount of time for the assembly of each of the compounds to the electrode surface.

Afterward, the PDMS channels are peeled from the chip, and both are gently rinsed with PBS, followed by deionized water, then blown dry with nitrogen. The channels are rotated 90° and placed back over the chip so that each channel now contains a counter electrode, a platinum reference electrode, and three working electrodes, each with a different surface functionalization.

RESULTS

A. Protein Impedance Data. PBS solutions containing either 50 μg/mL CRP, 5 μg/mL TNFα, or 5 μg/mL TNFβ are introduced across the sensors and allowed to interact with the surfaces for 15 min. Afterward, the channels are flushed with PBS solution to remove any loosely adsorbed molecules. Impedance spectroscopy data is taken using the same PBS solution containing the ferri-/ferrocyanide couple at a DC bias potential of −5 mV with an amplitude of 5 mV in the range of 10 000−0.1 Hz. Scans are taken before and after the proteins are introduced to the channels.

The impedance of the electrode system can be roughly modeled by using the Randles equivalent circuit, as shown in Scheme 1. The model includes the ohmic resistance of the solution (R_s); the double layer capacitance (C_d) resulting from the charged electrode surface and the ionic solution surrounding it; the charge transfer resistance (R_{ct}); and the Warburg impedance (W), which accounts for the diffusion of the redox species to and from the electrode. Plotting the impedance over a range of frequencies in a Nyquist plot for an electrode placed in an electrolyte results in a semicircular region at high frequencies, followed by a linear region at lower frequencies. Increasing values of R_{ct} increase the diameter of the semicircle; increasing values of C_d decrease the curvature. Thus, the model can be applied to the plotted data, and these parameters can be extracted. The addition of biomolecules to the electrode surface is expected to most strongly affect R_{ct}, the resistance of the redox compound's transfer of electrons to and from the surface. The mechanisms that cause either an increase or decrease in R_{ct} after assembly of biomolecules will be explained further in the Discussion section.

The change in impedance caused by each protein to the MCH surface is seen from the Nyquist plots in Figure 5. Part a displays a clear impedance increase after incubation with TNFα. Part b displays no measurable impedance change after incubation with TNFβ, and part c shows a clear decrease in impedance after incubation with CRP. Noise can be observed in some of the data at lower frequencies and is most likely caused by the long probe leads used to make contact to the chip as well as the small size of the electrodes used. These noise variations can be reduced through the use of a Faraday cage (a metal mesh) placed around the testing setup.

The change in impedance caused by each protein to the BSA surface is seen from the Nyquist plots in Figure 6. Each protein yielded only a slight increase in impedance after incubation with the BSA surface. This is attributed to BSA's known ability to reduce adsorption of other compounds to its surface and has been utilized by many groups for this reason, as previously mentioned. It should also be noted that the impedance of the BSA surface is much higher (larger R_{ct} value from the Randles circuit) than that of the MCH surface from Figure 5. This result is to be expected, since BSA is a much larger compound (MW = 70 000) than MCH (MW = 134) and should block more of the redox compound from interacting with the surface. This high impedance can also be used to explain the lack of a linear region in the Nyquist plot at lower frequencies. The 45° phase response at low frequencies occurs as a result of diffusion-dominated transport of the charge from the redox compound in solution. The BSA molecules provide enough of a physical barrier to the penetration of the redox compounds that diffusion has little overall effect on the measured impedance, and thus, the linear region is not present at lower frequencies.

The change in impedance caused by each protein to the PEG surface is seen from the Nyquist plots in Figure 7. For all three proteins studied, the impedance appears to increase greatly after incubation with the PEG-functionalized surface; however, it should be noted that the PEG formed an unstable monolayer during testing, as evidenced by the variations in its initial impedance. There also appears to be another semicircular region at high frequencies for the PEG layer on two of the sensors. This suggests a secondary electron transfer reaction taking place in the system from an unknown source. A full investigation of the PEG results is beyond the scope of this paper; however, future studies have been planned to utilize PEG compounds of various lengths

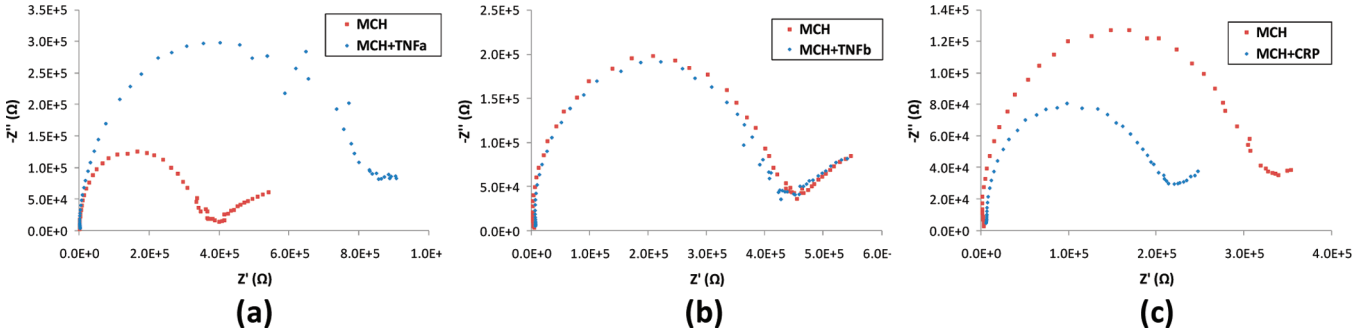

Figure 5. Impedance spectroscopy data for electrodes passivated with MCH followed by incubation for 15 min with (a) TNFα, (b) TNFβ, and (c) CRP.

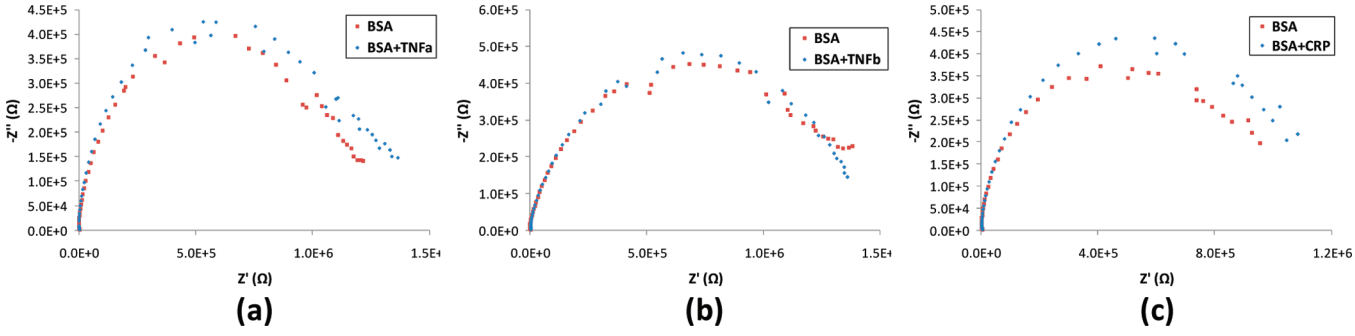

Figure 6. Impedance spectroscopy data for electrodes passivated with BSA, followed by incubation for 15 min with (a) TNFα, (b) TNFβ, and (c) CRP.

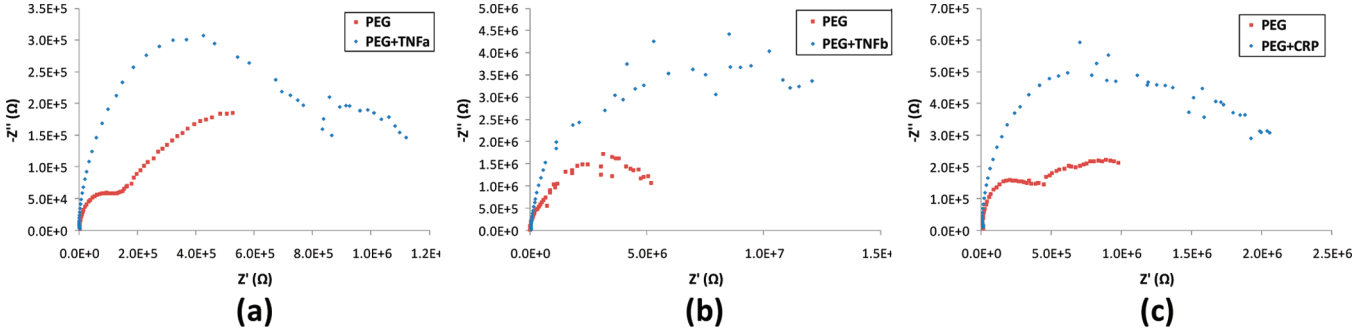

Figure 7. Impedance spectroscopy data for electrodes passivated with PEG, followed by incubation for 15 min with (a) TNFα, (b) TNFβ, and (c) CRP.

and with different functional head groups to better understand the results obtained in this study.

The values of R_{ct} and C_d for each surface and protein tested before and after incubation are shown in Table 1. These values were all extracted from the raw data presented in Figures 5−7. A higher starting R_{ct} value for electrodes covered in BSA vs those covered with MCH can be attributed to the greater size of BSA proteins vs the short-carbon-chain compound MCH, which increases the distance of the redox compound bulk concentration from the electrode surface. The higher C_d value for BSA vs MCH could be attributed to a higher dielectric effect caused by the presence of the BSA. The capacitance values show little variation (average percent change, 11%) following incubation with any of the three proteins for all surfaces.

Repeated measurements of both the MCH and BSA surfaces with all three proteins were performed using the device, and the percent change in R_{ct} was calculated as shown in Figure 8. The error bars designate one standard deviation with $n = 3$. This data can be used to discern noticeable trends among the interactions between the surfaces and proteins. TNFβ displayed very little impedance change for either surface, suggesting little to no adsorption occurred, and TNFα displayed the highest impedance increase for both surfaces. CRP consistently displayed a decrease in the impedance with MCH. The BSA surface displays only minor interactions with all three proteins over the course of numerous experiments. The data for the PEG surface is not included in this figure because of the instability of the layer. It is difficult to compare impedance spectra from various experiments with PEG because the model could not converge for much of the collected impedance data.

B. Refreshing Sensor Surface. Another advantage of having integrated electrical sensors is the ability to refresh the sensor

dx.doi.org/10.1021/ac200835s |*Anal. Chem.* 2011, 83, 5920–5927

Table 1. Values for the Charge Transfer Resistance (R_{ct}) and Double Layer Capacitance (C_d) for Each Protein and Surface Investigated[a]

		TNFα		TNFβ		CRP	
surface	incubation	R_{Ct}[b]	C_d[c]	R_{Ct}[b]	C_d[c]	R_{Ct}[b]	C_d[c]
MCH	before	3.38	6.31	4.16	5.20	2.78	5.46
	after	6.97	6.48	4.00	4.62	1.76	5.01
BSA	before	8.17	14.90	7.39	15.20	7.06	12.10
	after	9.20	12.60	7.66	16.50	8.25	10.30
PEG	before	1.16	9.43	13.30	4.01	3.59	5.58
	after	6.63	8.24	41.20	3.62	11.00	4.73

[a] Values are extracted from the impedance data displayed in Figures 5−7 fitted to the circuit model shown in Scheme 1. [b] R_{ct} ($\Omega \times 10^5$). [c] C_d ($F \times 10^{-9}$).

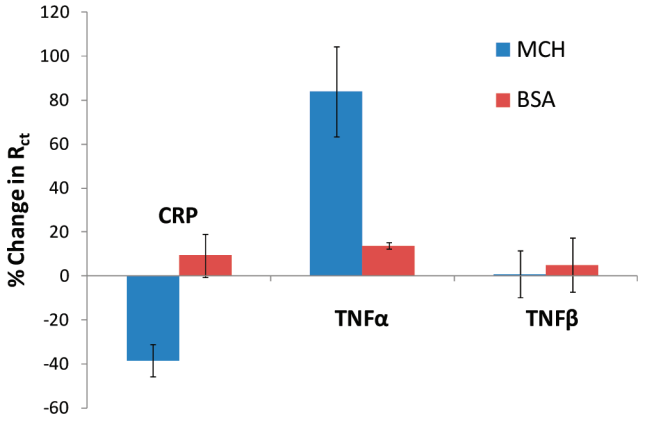

Figure 8. Percent change in R_{ct} for adsorption of each protein to both MCH and BSA. Clear trends can be determined, including the large impedance increase for TNFa on MCH and impedance decrease for CRP on MCH. All three proteins display roughly the same impedance change for a surface coated with BSA. Error bars designate one standard deviation, $n = 3$.

surface via an applied potential. Typically, an electrode surface is electrochemically cleaned by dipping the electrode into a 1 M sulfuric acid solution while potential is cycled vs a Ag/AgCl reference.[34] However, sulfuric acid is too caustic for use with PDMS, so a similar cleaning procedure has been achieved by cycling the potential applied to the working electrode well above and below the formal reduction potential of ferricyanide in PBS.

Figure 9 displays cyclic voltagrams of an electrode surface demonstrating passivation with a high concentration (1 mM) of PEG and subsequent regeneration of the current response due to electrochemical cleaning. PEG was chosen because of its high packing density at higher concentrations. The layer becomes so dense that there is little to no penetration of the ferricyanide to reach the electrode surface, as evidenced by the lack of any measurable current response after PEG binding in Figure 9. After electrochemically cycling the sensor surface between −0.8 and 0.8 V vs platinum, the current peaks are almost completely regenerated. This regeneration was observed for electrodes passivated with MCH and BSA, as well.

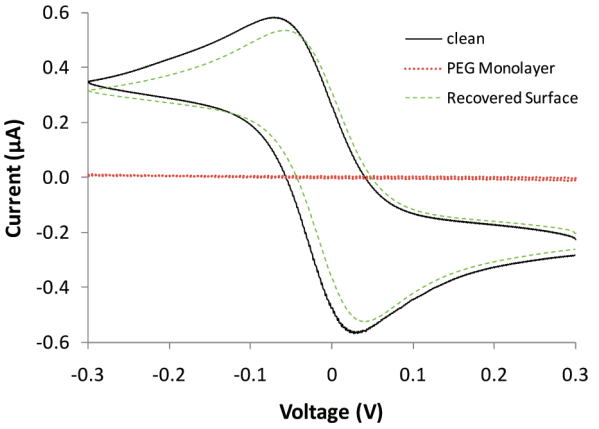

Figure 9. Cyclic voltammetry measurements of a blank electrode (solid), the response after incubation with PEG (dotted), and the final response after applying a high switching potential (0.8 to −0.8 V) to the electrode (dashed).

Scheme 2. Modification of the Randles Circuit To More Closely Model the Collected Impedance Data[a]

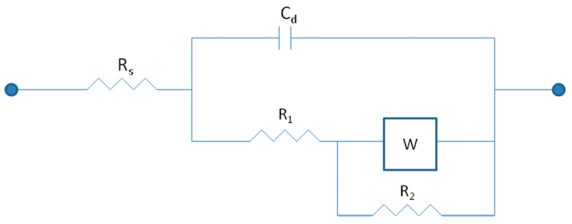

[a] The same R_s, C_d, and W from Scheme 1 are used, but the resistance contribution from R_{ct} has now been split among R_1 and R_2.

DISCUSSION

The functionalization compounds (MCH, BSA, PEG) and proteins (CRP, TNFα, TNFβ) used for this research were chosen to demonstrate the ability of the presented device to electrochemically probe an array of binding interactions. The device was successful in measuring impedance changes for each interaction. The mechanisms regarding both protein adhesion and the affect on the impedance include electrostatic interaction and steric stabilization. The impedance of the system is directly related to the ability of the charged redox compound to exchange electrons with the electrode surface. If the net surface charge is made to be either more positive or more negative, this will either better attract or repel the negative redox compound (in the case of the ferri-/ferrocyanide couple) in solution and affect the measured impedance accordingly. Steric stabilization describes the resistance of polymeric chains to being compressed and has been used to explain why PEG has been demonstrated to resist protein adsorption.[27]

The impedance results with MCH from Figure 5 demonstrate the aforementioned electrostatic effect well. Incubation with TNFα displays an impedance increase, and incubation with CRP decreases the impedance. The net charge polarity of each protein is different for the conditions used; that is, the amino acids expressed on the surface of TNFα provide a net negative charge at neutral pH (isoelectric point of 5.01), whereas those of CRP provide a net positive charge (isoelectric point of 9.2).[43]

dx.doi.org/10.1021/ac200835s |Anal. Chem. 2011, 83, 5920–5927

Table 2. Values for the Resistance Elements (R_1, R_2) and Double Layer Capacitance (C_d) for Each Protein and Surface Investigated[a]

		TNFα			TNFβ			CRP		
surface	incubation	R_1[b]	R_2[b]	C_d[c]	R_1[b]	R_2[b]	C_d[c]	R_1[b]	R_2[b]	C_d[c]
MCH	before	3.05	3.50	5.97	4.02	3.51	4.77	2.51	1.43	5.41
	after	4.66	4.75	6.24	3.85	3.44	4.51	1.45	1.23	4.85
BSA	before	2.31	11.20	11.70	0.67	15.72	10.91	4.66	7.35	10.48
	after	4.12	10.61	10.39	0.70	15.40	13.22	4.04	8.57	9.06
PEG	before	0.90	8.29	8.56	5.31	67.70	3.46	2.65	10.39	4.98
	after	3.56	8.31	7.13	16.60	153.81	3.27	6.79	17.34	4.34

[a] Values are extracted from the impedance data displayed in Figures 5−7 fitted to the circuit model shown in Scheme 2. [b] R_1, R_2 ($\Omega \times 10^5$). [c] C_d ($F \times 10^{-9}$).

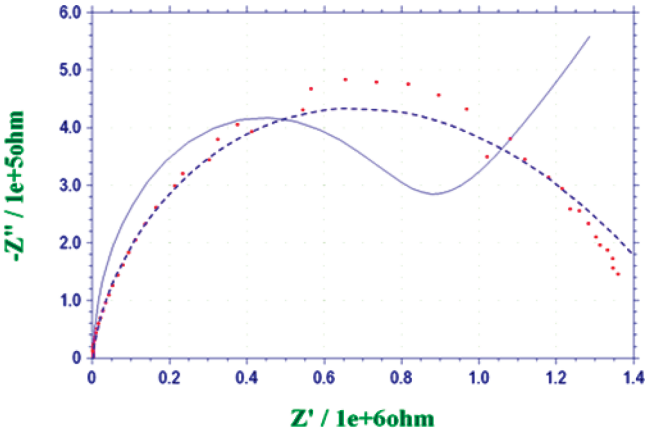

Figure 10. Impedance spectra for an electrode passivated with BSA, including the fitted curve for two circuit models. The solid line displays the fit using the Randles circuit from Scheme 1, and the dotted line displays the fit using the improved circuit from Scheme 2. The improved fit results in a 4× reduction of the fitting error.

The impedance changes suggest that both proteins interact with the hydroxyl head groups of the MCH and bind to the surface; however, the negatively charged TNFα causes repulsion of the ferricyanide, and the positively charged CRP attracts the ferricyanide, thus explaining the opposite impedance changes for each protein.

The device is very useful for helping one discover which surface modifications specific proteins show little to no interaction. TNFβ from Figure 5 does not cause any measurable impedance change to a MCH functionalized surface. This is an interesting result, given that it shares nearly 28% of its amino acid sequence with TNFα and both versions of TNF bind to the same receptors.[44] Neither TNFβ nor CRP adsorb to the electrode surface passivated with BSA. TNFα displays some increased impedance with a BSA passivated electrode as a result of its high repulsion of the redox compound, but the effect is far less than that observed with the MCH surface.

The values for the electron transfer resistance and double layer capacitance in Table 1 for each of the impedance measurements were obtained by fitting the data to the Randles model using the potentiostat's software program; however, this model is not always the most accurate way to describe every environmental situation. In our studies, the electrode surface was densely covered by the passivation compounds used, especially when using BSA. This can be observed in the Nyquist impedance plots from the lack of a linear region at low frequencies. The absence of this linear region suggests that the diffusion of the redox compound has been almost completely blocked by the surface passivation. To more accurately model this scenario, the circuit shown in Scheme 2 was utilized. A resistor (R_2) has been added in parallel with the Warburg impedance element. This resistance reduces the effect that the Warburg impedance has on the system and more accurately models a situation in which diffusion is not the dominant mechanism at lower frequencies.

The modeling of the charge transfer resistance has now been split among the two resistances, R_1 and R_2. The values of R_1, R_2, and C_d for each protein−surface interaction before and after incubation are shown in Table 2. Figure 10 displays how the circuit model in Scheme 2 better fits the raw impedance data than the conventional Randles circuit from Scheme 1. This impedance data is taken from an electrode passivated with BSA. A 4× reduction in the fitting error was achieved when using the circuit from Scheme 2 vs the circuit from Scheme 1. The average percent error for fitting all of the data collected was reduced from 8.1% to 6.5% for MCH-passivated surfaces, from 14.6% to 5.3% for BSA-passivated surfaces, and from 16.4% to 6.3% for PEG-passivated surfaces by using the improved circuit model.

CONCLUSION

A microfluidic platform with arrayed electrochemical sensors has been developed and tested by observing protein interactions with various surface types. The design allows the user to determine which sensors are functionalized with which material and ultimately to observe impedance changes at each surface when introduced to protein. The sensors were characterized using cyclic voltammetry measurements, and the interaction between a commonly studied bacterial gene regulator (CRP) and two cancer marker proteins (TNFα and TNFβ) with three modified electrode surfaces (MCH, BSA, and PEG) was studied using impedance spectroscopy. Each protein demonstrated a different impedance change with the MCH surface. None of the proteins changed the impedance of the surface passivated with BSA. The PEG layer proved to be too unstable for any definite conclusion. Future studies using the device to characterize protein adsorption onto various PEG structures have been planned to further explore its use as a passivation material for impedance-based experiments.

Reprogrammability of the sensor surface by applying a high sweeping potential has also been demonstrated. Furthermore, the microfluidic design requires drastically reduced sample volumes vs conventional detection techniques, and the arrayed format reduces the time required to probe interactions among numerous species. Although the current design utilizes 9 sensors per device, this number can easily be scaled up while keeping the device footprint roughly the same, which will lead to even higher throughput for surface adsorption characterization. The device could also be used to quantify the increase in the signal-to-noise ratio in the impedance study of a specific affinity assay for various passivation materials. The ability to quickly characterize protein interactions with many different surfaces in the same device can help future researchers understand how to improve the selectivity and nonadsorption behavior for the next generation of biosensors and biomedical devices.

AUTHOR INFORMATION

Corresponding Author
*E-mails: (P.H.D.) pdykstra@umd.edu, (R.G.) ghodssi@umd.edu.

ACKNOWLEDGMENT

The authors acknowledge the R. W. Deutsch Foundation and National Science Foundation Emerging Frontiers in Research and Innovation (EFRI) for financial support. The authors also thank the Maryland Nanocenter and its Fablab for cleanroom facility support. The authors also thank Dr. James Sumner from the Army Research Laboratory.The authors also thank the Defense Threat Reduction Agency (DTRA) and the Office of Naval Research (ONR).

REFERENCES

(1) He, X.; Yuan, R.; Chai, Y.; Shi, Y. *J. Biochem. Biophys. Methods* **2008**, *70*, 823–829.
(2) Pavlovic, E.; Lai, R. Y.; Wu, T. T.; Ferguson, B. S.; Sun, R.; Plaxico, K. W.; Soh, H. T. *Langmuir* **2008**, *24*, 1102–1107.
(3) Qureshi, A.; Niazi, J. H.; Kallempudi, S.; Gurbuz, Y. *Biosens. Bioelectron.* **2010**, *25*, 2318–2323.
(4) Xu, X.; Zhang, S.; Chen, H.; Kong, J. *Talanta* **2009**, *80*, 8–18.
(5) Zheng, G.; Patolsky, F.; Cui, Y.; Wang, W. U.; Lieber, C. M. *Nat. Biotechnol.* **2005**, *23*, 1294–1301.
(6) Cai, H.; Lee, T.M.-H.; Hsing, I.-M. *Sens. Actuators, B* **2006**, *114*, 433–437.
(7) Chang, H.; Li, J. *Electrochem. Commun.* **2009**, *11*, 2101–2104.
(8) Fan, R.; Vermesh, O.; Srivastava, A.; Yen, B. K. H.; Qin, L.; Ahmad, H.; Kwong, G. A.; Liu, C.-C.; Gould, J.; Hood, L.; Heath, J. R. *Nat. Biotechnol.* **2008**, *26*, 1373–1378.
(9) Harper, J. C.; Polsky, R.; Wheeler, D. R.; Dirk, S. M.; Brozik, S. M. *Langmuir* **2007**, *23*, 8285–8287.
(10) Lin, C.-C.; Chen, L.-C.; Huang, C.-H.; Ding, S.-J.; Chang, C.-C.; Chang, H.-C. *J. Electroanal. Chem.* **2008**, *619*−*620*, 39–45.
(11) Ban, C.; Chang, S.; Park, D.-S.; Shim, Y.-B. *Nucleic Acids Res.* **2004**, 32.
(12) Cheng, A. K. H.; Sen, D.; Yu, H.-Z. *Bioelectrochemistry* **2009**, *77*, 1–12.
(13) Rodriguez, M. C.; Kawde, A.-N.; Wang, J. *Chem. Commun.* **2005**, 4267–4269.
(14) Ostuni, E.; Yan, L.; Whitesides, G. M. *Colloids Surf. B* **1999**, *15*, 3–30.
(15) Prime, K. L.; Whitesides, G. M. *J. Am. Chem. Soc.* **1993**, *115*, 10714–10721.
(16) Ratner, B.D.; Hoffmann, A.S.; Schoen, F.J.; Lemons, J.E. *Biomaterials Science. An Introduction to Materials in Medicine*; Academic Press: New York, 1996.
(17) Alkan, M.; Demirbaş, Ö.; Doğan, M.; Arslan, O. *Microporous Mesoporous Mater.* **2006**, *96*, 331–340.
(18) Price, M. E.; Cornelius, R. M.; Brash, J. L. *Biochim. Biophys. Acta* **2001**, *1512*, 191–205.
(19) Scott, E. A.; Nichols, M. D.; Cordova, L. H.; George, B. J.; Jun, Y.-S.; Elbert, D. L. *Biomaterials* **2008**, *29*, 4481–4493.
(20) Mao, Y.; Wei, W.; Peng, H.; Zhang, J. *J. Biotechnol.* **2001**, *89*, 1–10.
(21) Menz, B.; Knerr, R.; Göpferich, A.; Steinem, C. *Biomaterials* **2005**, *26*, 4237–4243.
(22) Ogi, H.; Fukunishi, Y.; Nagai, H.; Okamoto, K.; Hirao, M.; Nishiyama, M. *Biosens. Bioelectron.* **2009**, *24*, 3148–3152.
(23) Saito, N.; Matsuda, T. *Mater. Sci. Eng., C* **1998**, *6*, 261–266.
(24) Doan, T. T.; Vargo, M. L.; Gerig, J. K.; Gulka, C. P.; Trawick, M. L.; Dattelbaum, J. D.; Leopold, M. C. *J. Colloid Interface Sci.* **2010**, *352*, 50–58.
(25) Hedlund, J.; Lundgren, A.; Lundgren, B.; Elwing, H. *Sens. Actuators, B* **2009**, *142*, 494–501.
(26) Xie, Q.; Zhang, Y.; Xu, M.; Li, Z.; Yuan, Y.; Yao, S. *J. Electroanal. Chem.* **1999**, *478*, 1–8.
(27) Mrksich, M.; Whitesides, G. M. *Annu. Rev. Biophys. Biomol. Struct.* **1996**, *25*, 55–78.
(28) Sapsford, K. E.; Ligler, F. S. *Biosens. Bioelectron.* **2004**, *19*, 1045–1055.
(29) Mitchell, P. *Nat. Biotechnol.* **2002**, *20*, 225–229.
(30) Narakathu, B. B.; Atashbar, M. Z.; Bejcek, B. E. *Biosens. Bioelectron.* **2010**, *26*, 923–928.
(31) Varshney, M.; Li, Y.; Srinivasan, B.; Tung, S. *Sens. Actuators, B* **2007**, *2007*, 99–107.
(32) Yang, L. *Talanta* **2009**, *80*, 551–558.
(33) Ma, C.; Hou, Y.; Liu, S.; Zhang, G. *Langmuir* **2009**, *25*, 9467–9472.
(34) McEwen, G. D.; Chen, F.; Zhou, A. *Anal. Chim. Acta* **2009**, *643*, 26–37.
(35) Sumner, J. J.; Plaxico, K. W.; Meinhart, C. D.; Soh, H. *Proc. SPIE* **2005**, *6007*, 600706.
(36) Yang, Z.; Galloway, J. A.; Yu, H. *Langmuir* **1999**, *15*, 8405–8411.
(37) Dai, Z.; Serban, S.; Ju, H.; Murr, N. E. *Biosens. Bioelectron.* **2007**, *22*, 1700–1706.
(38) Meagher, R. J.; Hatch, A. V.; Renzi, R. F.; Singh, A. K. *Lab Chip* **2008**, *8*, 2046–2053.
(39) Krakow, J. S.; Pastan, I. *Proc. Natl. Acad. Sci. U.S.A.* **1973**, *70*, 2529–2533.
(40) Lawson, C. L.; Swigon, D.; Murakami, K. S.; Darst, S. A.; Berman, H. M.; Ebright, R. H. *Curr. Opin. Struct. Biol.* **2004**, *14*, 1–11.
(41) Kamali-Sarvestani, E.; Merat, A.; Talei, A.-R. *Cancer Lett.* **2005**, *223*, 113–119.
(42) Polsky, R.; Harper, J. C.; Wheeler, D. R.; Dirk, S. M.; Arango, D. C.; Brozik, S. M. *Biosens. Bioelectron.* **2008**, *23*, 757–764.
(43) Harman, J. G. *Biochim. Biophys. Acta* **2001**, *1547*, 1–17.
(44) Aggarwal, B.; Reddy, S. *Guidebook to Cytokines and Their Receptors*; Oxford University Press: New York, 1994.

NOTE ADDED AFTER ASAP PUBLICATION

This paper was published on the Web on June 29, 2011, with an error in the author affiliations. The corrected version was reposted on July 5, 2011.